The Radiative and Geometric Properties of Melting First-Year Sea Ice

Nathan J. M. Laxague[1†], Christopher J. Zappa[1], Andrew R. Mahoney[2], John Goodwin[3], Cyrus Harris[3], Robert E. Schaeffer[3], Roswell Schaeffer Sr.[3], Sarah Betcher[4], Donna D.W. Hauser[5], Carson R. Witte[1], Jessica M. Lindsay[6], Ajit Subramaniam[1], Kate E. Turner[7], Alex Whiting[8]

[1]Lamont-Doherty Earth Observatory, Columbia University, Palisades, NY, USA, [2]Geophysical Institute, University of Alaska Fairbanks, Fairbanks, AK, USA, [3]Community of Kotzebue, Kotzebue, AK, USA, [4]Farthest North Films, Homer, AK, USA, [5]International Arctic Research Center, University of Alaska Fairbanks, Fairbanks, AK, USA, [6]University of Washington Seattle Campus, Seattle, WA, USA, [7]National Institute of Water and Atmospheric Research, Wellington, New Zealand, [8]Native Village of Kotzebue, Kotzebue, AK, USA

Corresponding author: Nathan Laxague (Nathan.Laxague@unh.edu)

†Current affiliation: Department of Mechanical Engineering and Center for Ocean Engineering, University of New Hampshire, Durham, NH, USA

Key Points:

- High-resolution aerial radiometric observations were made over heavily-degraded first-year sea ice in Arctic Alaska.
- Large regions of blue-green ice were observed to be associated with strong net solar irradiance into the surface.
- Snowy ice features increased in reflectance with size up to a critical scale, with no size dependence beyond that.

Abstract

In polar regions, sea ice is a crucial mediator of the interaction between earth's atmosphere and oceans. Its formation and breakup is intimately connected with local weather patterns and larger-scale climatic processes. During the spring melt and breakup period, snow-covered ice transitions to open water in a matter of weeks. This has a profound impact on the use of sea ice in coastal Arctic regions by Indigenous People, where activities such as hunting and fishing are central to community livelihood. In order to investigate the physical phenomena at the heart of this process, a set of targeted, intensive observations were made over Spring sea ice melt and breakup in Kotzebue Sound, Alaska. This program is part of the Ikaaġvik Sikukun project, a collaborative effort in which an Indigenous Elder advisory council from Kotzebue and scientists participated in co-production of hypotheses and observational research, including a stronger understanding of the physical properties of sea ice during spring melt. Data were collected using high-endurance, fixed-wing uncrewed aerial vehicles (UAVs) containing custom-built scientific payloads. Here we present the results of these measurements. Repeated flights over the measurement period captured the early stages of the transition from a white, snow-covered state to a broken up, bare/blue-green state. We found that the reflectivity of a surface type depends on the size and shape of the features which constitute it. Specifically, large bare blue-green ice features were found to be least reflective, while large snowy/white ice features were found to be most reflective.

Plain Language Summary

We performed a series of airborne observations aimed at describing the types and sizes of features that are most strongly connected to the absorption of solar energy. We found that feature size and shape affects the tendency of sea ice to absorb solar energy and melt. Specifically, we found that large patches of bare blue-green ice are the most strongly absorptive, and that as regions of snowy white ice become smaller, they become less reflective.

1 Introduction

Sea ice is an essential feature of the polar oceans, looming large as both visual wonder and geophysical presence. The standard processes of air-sea interaction---whereby fluxes of momentum, heat, and mass are mediated by turbulent flow past an undulating interface---are fundamentally transformed by the presence of sea ice which attenuates (or completely suppresses) surface waves and wind-forced currents. However, there is perhaps no sea ice-related geophysical effect more stark than its alteration of the solar radiative balance. Whereas the ice-free ocean tends to reflect less than 10% of incoming solar radiation, the myriad forms of snow and ice at various stages of melt and degradation will reflect between 15-90% of incoming solar radiation. Broadband albedo, the ratio of wavelength-integrated reflected solar irradiance to incident solar irradiance, is strongly dependent on the surface state of the ice (Perovich et al., 1998), with fractional cover of snow on the surface the single most important determinant of high albedo (Yackel et al., 2000). The formation of melt ponds on the surface of sea ice alters surface radiative properties, lowering surface albedo (Barber & Yackel, 2010) and increasing the transmittance of light through the ice into the underlying sea (Ehn et al., 2011; Frey et al., 2011; Light et al., 2015). It has long been known that solar radiative heat flux into the sea ice surface contributes to melting, reducing its reflectance and increasing its susceptibility to further degradation (Budyko, 1969). This phenomenon, known as the ice-albedo feedback, is understood to be a key component of the Earth's climatic variability. The rapid decline in sea ice extent in the recent past (Brennan et al.,

2020) has led to an aggregate scale change in surface albedo as ice melts completely and is replaced by open water. Additionally, a widespread decline in Arctic sea ice thickness has been observed over the past half-century (Kwok & Rothrock, 2009). This is largely due to another feedback: as sea ice thins, it reflects less solar radiation (Lu et al., 2016) and allows for greater transmission of light (Light et al., 2008). This in turn results in increased ocean heat and enhanced melting of the sea ice bottom (Planck et al., 2020).

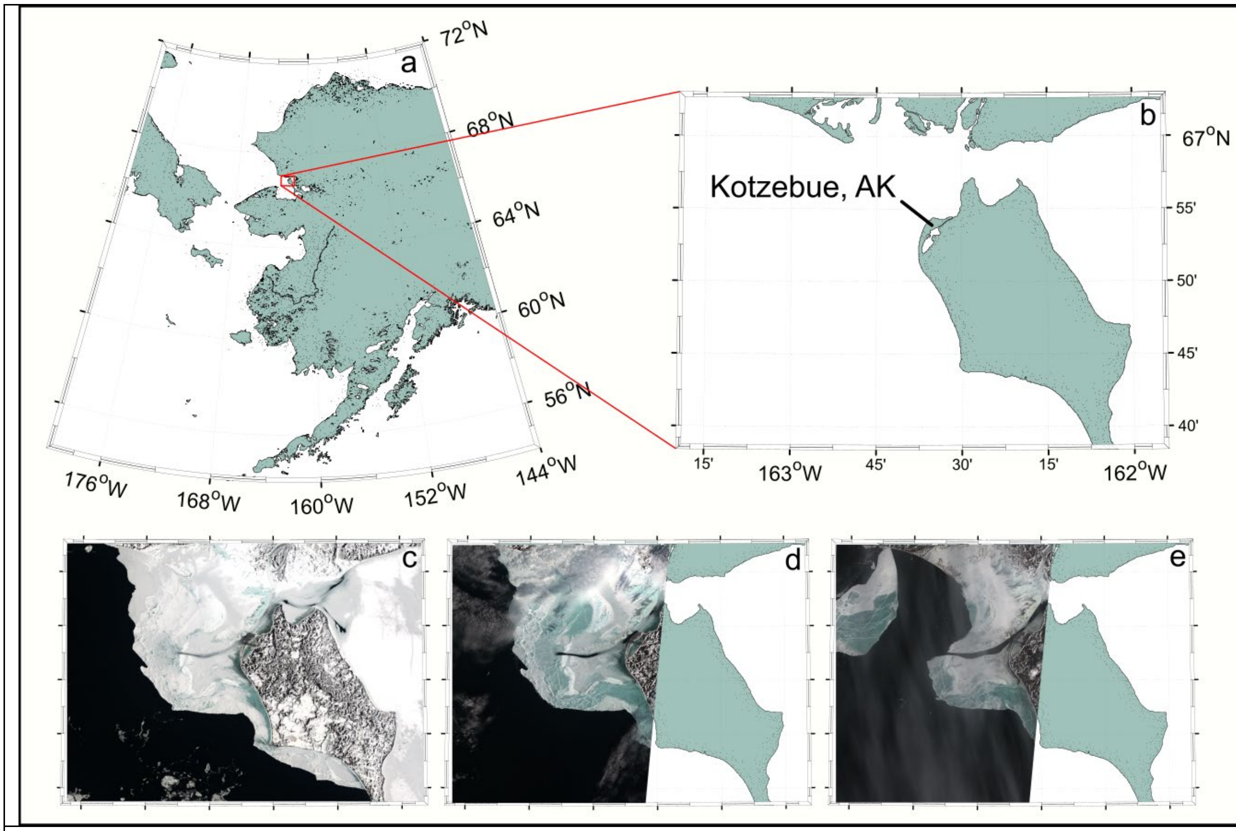

Figure 1: Map of **a** Alaska, **b** Kotzebue Sound, and three consecutive satellite overpasses showing the change of sea ice color and extent during May of 2019: **c** 5/6/2019, **d** 5/9/2019, **e** 5/14/2019.

Recent changes to the thickness, surface state, and overall extent of sea ice have yielded a dramatic increase in the absorption of solar heat in the Arctic Ocean (Perovich & Polashenski, 2012). This has resulted in the Arctic warming at nearly four times the global average rate (Rantanen et al., 2022), a phenomenon named Arctic amplification. There is abundant evidence that this is due to the diminishment of sea ice cover and thickness (Dai et al., 2019; Perovich et al., 2020; Screen & Simmonds, 2010). All of these trends have led to the Arctic system becoming far less resilient to change than it was decades ago (Overland, 2020). The consequences of these effects are most concrete, immediate, and stark for Indigenous Arctic communities who exist among the sea ice and often rely upon it as part of their way of life (Gearheard et al., 2013). For decades, the melt season has been trending to occur sooner and last for longer each year (Markus et al., 2009; Stroeve et al., 2014), threatening long-practiced Indigenous traditions such as seasonal hunts (Hauser et al., 2021).

In order to improve our understanding of the processes which drive these changes, there is a need for new field observations which quantify surface fluxes in high-latitude environments (Bourassa et al., 2013). So-called 'process' studies which target particular physical phenomena are particularly illuminating (Carmack et al., 2015). When conducting research on adaptation to climate change, it is valuable to move from an extractive (David-Chavez & Gavin, 2018) framework to one of co-production and stakeholder engagement (Klenk et al., 2017). The co-production of knowledge with local research partners is at its most effective when it is both iterative and interactive (Bremer et al., 2019), incorporating the needs of the community with an understanding of global-scale challenges (Eicken et al., 2021). This shift in mindset benefits the local communities most directly impacted by the processes being studied- but it also benefits the scientific research itself, with Indigenous Knowledge-holders providing key insights into local dynamics (Eicken, 2010), especially when equity between Indigenous People and scientists is a key component of the co-production framework (Yua et al., 2022).

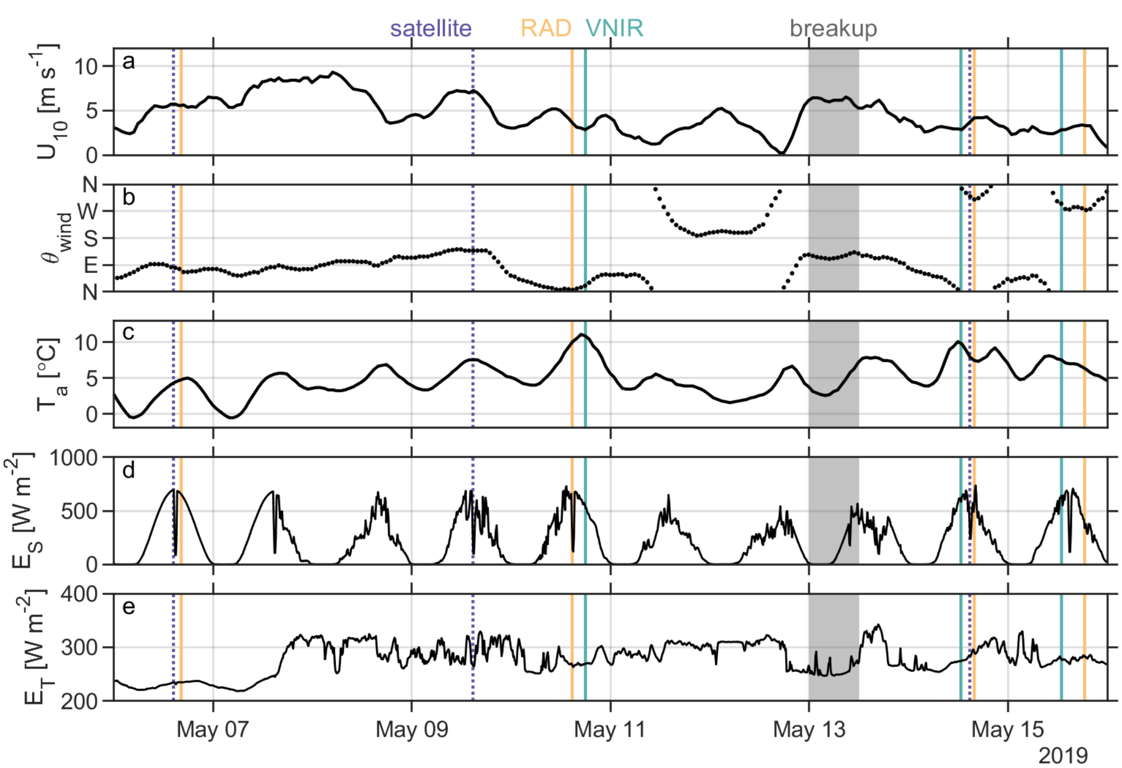

Figure 2: Environmental conditions during field campaign: **a** wind speed, **b** wind direction (coming-from convention), **c** air temperature, **d** downwelling solar irradiance, and **e** downwelling thermal irradiance. Wind/air measurements were made at Kotzebue Ralph Wien Airport, while radiative measurements were made at the U.S. Fish & Wildlife Service bunkhouse. Vertical lines indicate times of satellite overpasses (dotted violet), UAV flights with "RAD" payload (solid orange), UAV flights with "VNIR" payload (solid teal); gray shaded region denotes approximate time of major sea ice breakup.

The present study arose as part of the Ikaaġvik Sikukun project, a collaborative effort of knowledge co-production and observational research completed by an Indigenous Elder advisory council (study co-authors J.G., C.H., R.J.S., and R.S., Sr.) from Kotzebue, AK (Figure 1) and an interdisciplinary team of scientists. This project was community-involved from the outset, with the initial stage of collaboration centered around the generation of driving research questions largely focused on understanding the physical and biological changes associated with sea ice loss in Kotzebue Sound (Hauser et al., 2021; Lindsay et al., 2023; Mahoney et al., 2021; Witte et al., 2021). In many coastal regions, the onset of sea ice breakup is associated with a seasonal hunting period; in Kotzebue Sound, the Qikiqtaġruŋmiut hunt of *ugruk* (bearded seal) coincides with the breakup of sea ice. The details of this connection—and of our co-production of knowledge approach—is described in more detail by (Hauser et al., 2021). These factors were to be investigated using a variety of in situ, satellite, and uncrewed airborne observations. It is the latter set of high-resolution observations made from a series of flights throughout a period of advanced melt that form the basis of the present study.

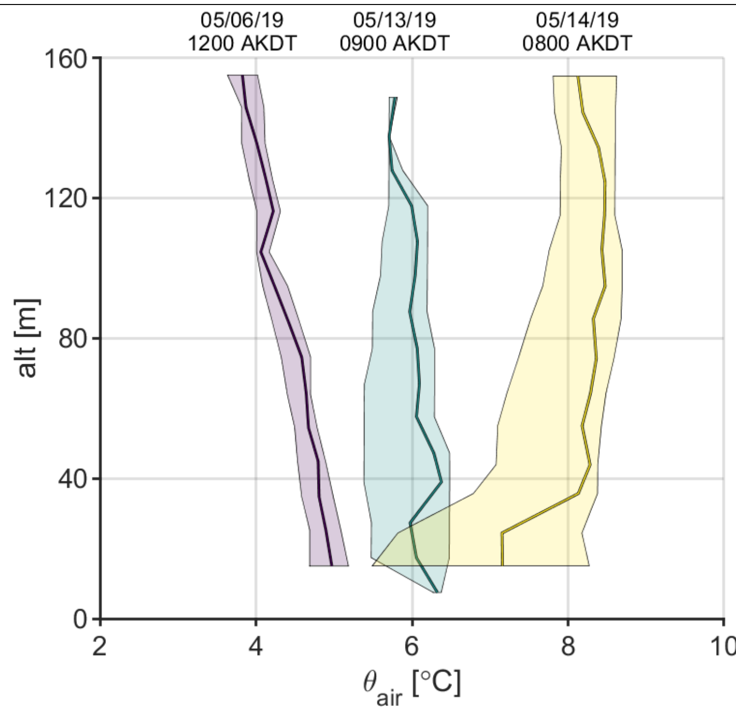

Figure 3: Potential temperature soundings taken from three flight ascent/descent patterns, one pre-breakup (May 6th, 2019) and two post-breakup (May 13th and 14th, 2019). Dark curves mark the mean profiles, while shaded regions represent the interdecile range of potential temperature variation. Hour of ascent (AKDT - Alaska Daylight Time) is given below date at top of figure.

Satellite images of Kotzebue Sound taken during our field observational campaign (Figure 1) show that the region's landfast sea ice appeared mostly blue-green by 5/9, with a major breakup event occurring between 5/13 and 5/14. Several important physical parameters are shown as stacked timeseries in Figure 2, with vertical lines indicating the timing of satellite overpasses and UAV flights (with the "RAD" and "VNIR" payloads, to be defined in section 2). These were obtained from land-based instrumentation: air temperature and wind velocity data from the meteorological station at Kotzebue Ralph Wien Airport (station PAOT); downwelling hemispheric radiative fluxes from a pair of Kipp & Zonen sensors (pyranometer and pyrgeometer) mounted on the rooftop of the U.S. Fish and Wildlife office. For the majority of our observational period, the sky was quite cloudy- this can be seen in the downwelling radiative flux time series of Figure 2, with high thermal irradiance and spottiness in solar irradiance (that is, departure from its characteristic bell-shaped diurnal behavior). The major landfast ice breakup event (indicated by the gray shaded region on Figure 2) was preceded by a rapid transition in the wind forcing, with onshore wind of

5 m/s giving way to offshore wind of 7 m/s. This transition in atmospheric conditions extended well into the atmospheric boundary layer (Figure 3).

2 Methods

2.1 UAV-based radiometry

For this work, we deployed uncrewed aerial vehicles (UAVs) equipped with specialized payloads for sensing downwelling (sky-leaving) and upwelling (surface-leaving) radiative fluxes in solar/shortwave and thermal/longwave bands. These sensors are listed below in table 1.

Quantity	Dimensions	Symbol	Sensor	Payload & Orientation	Spectral Sensitivity	Surface Spatial Resolution
Thermal irradiance	W/m^2	E_T	Hukseflux IR02 Pyrgeometer	RAD, up & down	4.5 – 40 µm	N/A
Solar irradiance	W/m^2	E_S	Hukseflux SR03 Pyranometer	RAD, up & down	285 – 3000 nm	N/A
Solar spectral irradiance	$W/m^2/nm$	$E_S(\lambda)$	OceanOptics USB2000 Irradiance Spectrometer	VNIR, up	200 – 1100 nm	N/A
Solar spectral radiance	$W/m^2/nm/sr$	$L_S(\lambda)$	Headwall Micro-HyperSpec VNIR A-Series Imaging Spectrometer	VNIR, down	400 – 1000 nm	57 cm @ 1000 m altitude

Table 1: Inventory of radiative measurements made via UAV, including the spectral sensitivity and surface spatial resolution.

The details of the UAS deployed during our field operations are provided by (Zappa et al., 2020); what follows here is a summary of the elements most relevant to the present study. Each UAV carried in its nosecone a "Base" payload (holding the core power and data management systems) and one of a number of modular payloads which allowed for specialized sensor depoloyment. The RAD and VNIR payloads were deployed for observing the radiative properties of the sea ice; their core onboard sensors are listed in table 1. The RAD payload contained up and down-looking Hukseflux model IR-02 pyrgeometers to measure thermal irradiance and up and down-looking Hukseflux model SR-03 pyranometers to measure solar irradiance, all sampled at 1 Hz. The VNIR payload contained an upward-looking Ocean Optics model USB2000+ spectrometer to measure downwelling visible and near-infrared spectral irradiance and a downward-looking Headwall Micro-Hyperspec imaging spectrometer to measure upwelling visible and near-infrared spectral radiance, all sampled at 25 Hz. The Headwall imaging spectrometer is a 'pushbroom' sensor, with each image 'frame' corresponding to 1004 cross-track pixels (at 0.032° IFOV) and 1004 spectral wavelengths (at 1.85 nm spectral resolution); of the 1004 spectral measurements, 216 fell within the wavelength range of 400-800 nm used for the analysis here. Each UAV's Base payload held an onboard inertial navigation unit (INU) comprised of a GPS receiver and an inertial measurement unit (IMU); a complementary ground station allowed for differential GPS post-processing. After each flight, all GPS and IMU data were combined via tightly-coupled processing, providing an integrated TSPI (time space position information) solution with centimeter-scale (±1 cm horizontal, ±2 cm vertical) position accuracy and 0.01° attitude accuracy.

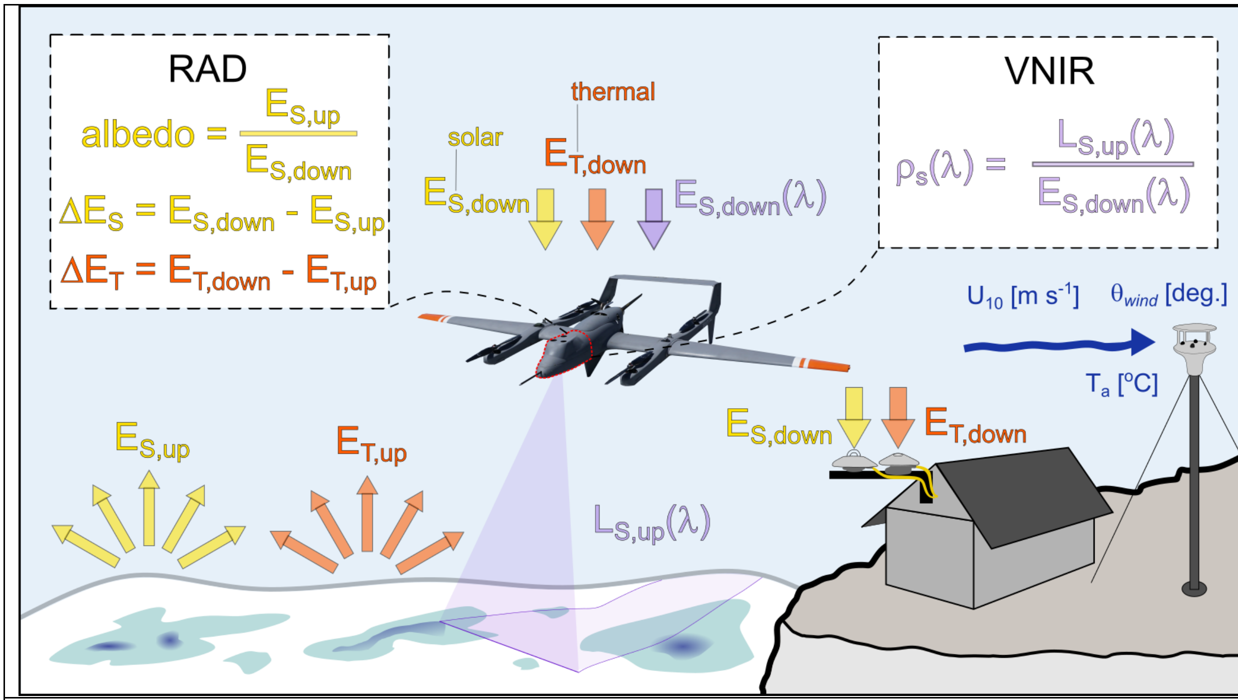

Figure 4: Depiction of fixed and aerial observational platforms, with arrows indicating radiative fluxes. Red dashed region on UAV indicates modular nosecone, with two red dashed boxes showing the measurement capabilities of two payloads: "RAD" payload, with upward/downward-looking pyranometers and pyrgeometers for characterizing upwelling and downwelling thermal and solar radiative fluxes; "VNIR" payload, with a downward-looking hyperspectral pushbroom imager and upward/downward-looking spectrometers for characterizing the spectral surface reflectance. Downwelling thermal and solar radiative fluxes were also measured from a rooftop station at the U.S. Fish and Wildlife Service bunkhouse. Wind speed, direction, and air temperature were measured from a meteorological station at Kotzebue Ralph Wien Airport.

It has been standard practice to separate sea ice features into distinct categories (e.g., snow, bare ice, melt ponds) and measure spectral albedo over those regions (Grenfell & Perovich, 1984, 2004; Perovich, Grenfell, et al., 2002). The relatively high altitude of our measurements rendered the hemispheric observations of the RAD payload too coarse to parse the radiative signatures of individual feature types. Given an altitude of 150 m, and the assumption that our hemispheric radiometers are ideal cosine collectors, we estimate that 90% of the signal originates from a region below the aircraft with diameter of 270 m. In order to complement these observations, VNIR payload performed measurements of sea ice spectral radiance, allowing for discernment of radiative characteristics at decimeter-scale spatial resolution.

The irradiance data obtained via sensors on the RAD payload were used to compute net solar irradiance, net thermal irradiance, and shortwave albedo (Figure 4). The downwelling spectral irradiance and upwelling spectral radiance data obtained via sensors on the VNIR payload were used to compute the spectral surface reflectance (Figure 4). The mean surface VNIR reflectance and broadband albedo observed along the track of each of the UAV flights are shown in Figure 5. Note that the surface reflectance measurements are localized in space (no more than 250 meters on either side of the flight track) while the albedo measurements were obtained via hemispheric sensors, integrating information from a far broader spatial region. Care was taken to ensure that ambient radiative conditions did not differ too greatly from one flight to the next. As shown in the time series of Figure 2, the incoming irradiance did not vary greatly across the VNIR flights (E_S = 570±50 W m^{-2}, E_T = 275±5 W m^{-2}). The disparate tracks from one flight day to the next resulted from rapidly-changing surface conditions; for the first two sets of flights, RAD and VNIR payloads followed the same flight paths. However, by 5/15, the degradation of the sea ice surface advanced to the point that our visual observer could not maintain line of sight with the aircraft, resulting in different flight plans for the RAD and VNIR payloads on that day.

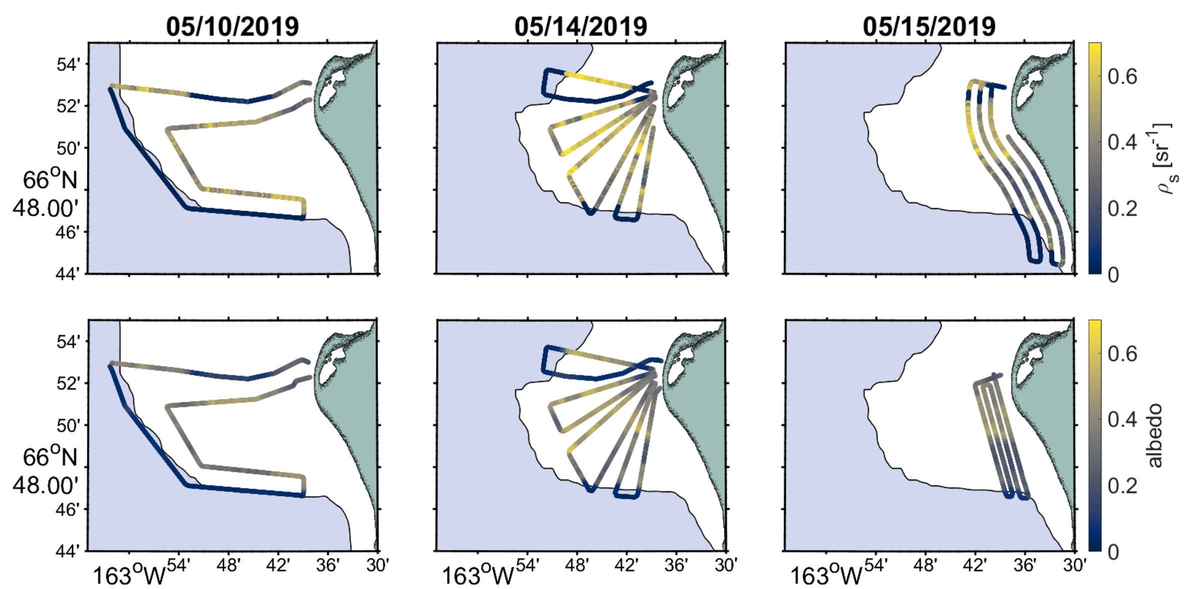

Figure 5: Flight tracks colored by data products of three days of operation with RAD and VNIR payloads (RAD only on 5/6/2019). Each flight day is confined to a column; each row consists of a single variable type (wavelength-averaged surface reflectance and broadband surface albedo, respectively). The green region indicates the Baldwin Peninsula, the white region indicates landfast ice, and the blue region indicates open water in Kotzebue Sound.

2.2 Sea ice surface feature identification and processing

Surface reflectance data obtained from the VNIR payload were georeferenced according to the aircraft's attitude and position from the tightly-coupled TSPI solution. At a flight altitude of 1000 m, the total position error of each georeferenced radiance observation was estimated to be <20 cm, smaller than the 57 cm ground sample distance (table 1). The 'pushbroom' processing is most readily described visually; please see appendix Figure A1 for a step-by-step view of the georeferencing.

The calibrated surface reflectance maps were bin-averaged in wavelength space with a spectral width of 5 nm; this provided an improvement to signal-to-noise ratio, especially for measurements in the violet and near-infrared ranges. Given that our principal interest lay in fixed features on sea ice, the next major step taken was to exclude regions of open water; these were identified as regions for which the mean spectral reflectance was less than 0.05. There is a wide range of surface classification schemes available given imagery of the sea ice surface-- even RGB or panchromatic imagery (Wright & Polashenski, 2018).

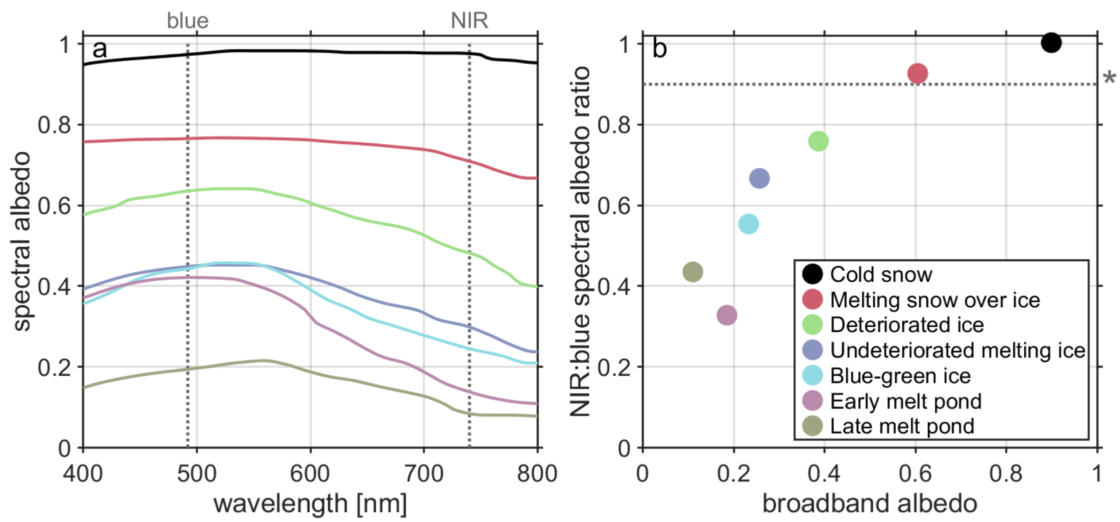

Figure 6: Spectral albedo (**a**) and the ratio between the spectral albedo in the near-infrared (NIR) and blue, or NIR:B (**b**) for a variety of classifications of first-year sea ice, organized by broadband albedo. Data shown in (**a**) were taken from (Perovich, 2017) and used to compute quantity shown in (**b**). Asterisk in panel (**b**) indicates a NIR:blue ratio of 0.9.

Given our hyperspectral visible and near-infrared observations of the surface, we are able to perform classification based on surface radiative properties. The approach chosen here was informed by the surface-dependent spectral albedo measurements of (Perovich, 2017) shown in Figure 6a. The ratio between surface reflectance in the near-infrared (740±10 nm) and blue (490±10 nm) visualized in Figure 6b- hereafter "NIR:B"- provides a reasonable separation point between spectrally flat (NIR:B~1) features of sea ice often characterized by snow cover and the blue/green features associated with a more advanced stage of melt (NIR:B<1). A demonstration of this partitioning is provided in Figure 7.

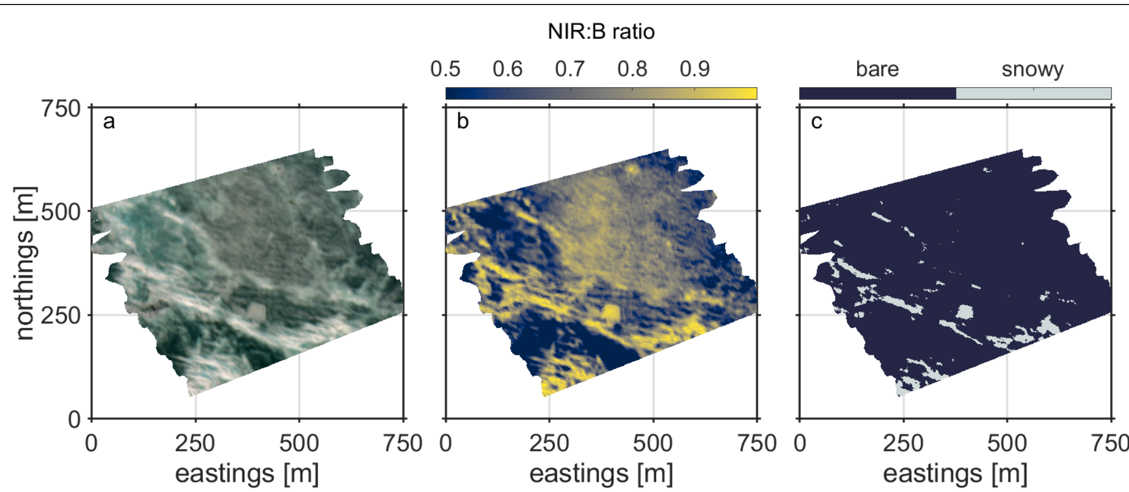

Figure 7: (**a**) Color mosaic produced from the red, green, and blue channels of ρ_s. (**b**) Ratio of the NIR and blue channels of ρ_s, (NIR:B). (**c**) Binarized frame showing separation into 'bare' and 'snowy' portions.

As indicated by Figure 6, partitioning the surface at a NIR:B value of 0.9 will bundle together bare ice with ponded ice. A second step of separation is required in order to parse melt ponds from the bare ice regions identified via the NIR:B approach. For this, we turned to the technique of (König & Oppelt, 2020), whereby the *slope* of the spectral reflectance in the near-infrared may be interpreted to infer the melt pond depth. The combined two-layer processing involves a check for melt ponds (which are then excluded from further partitioning) followed by a thresholding along the NIR:B value of 0.9. A demonstration of this processing is shown in Figure 8.

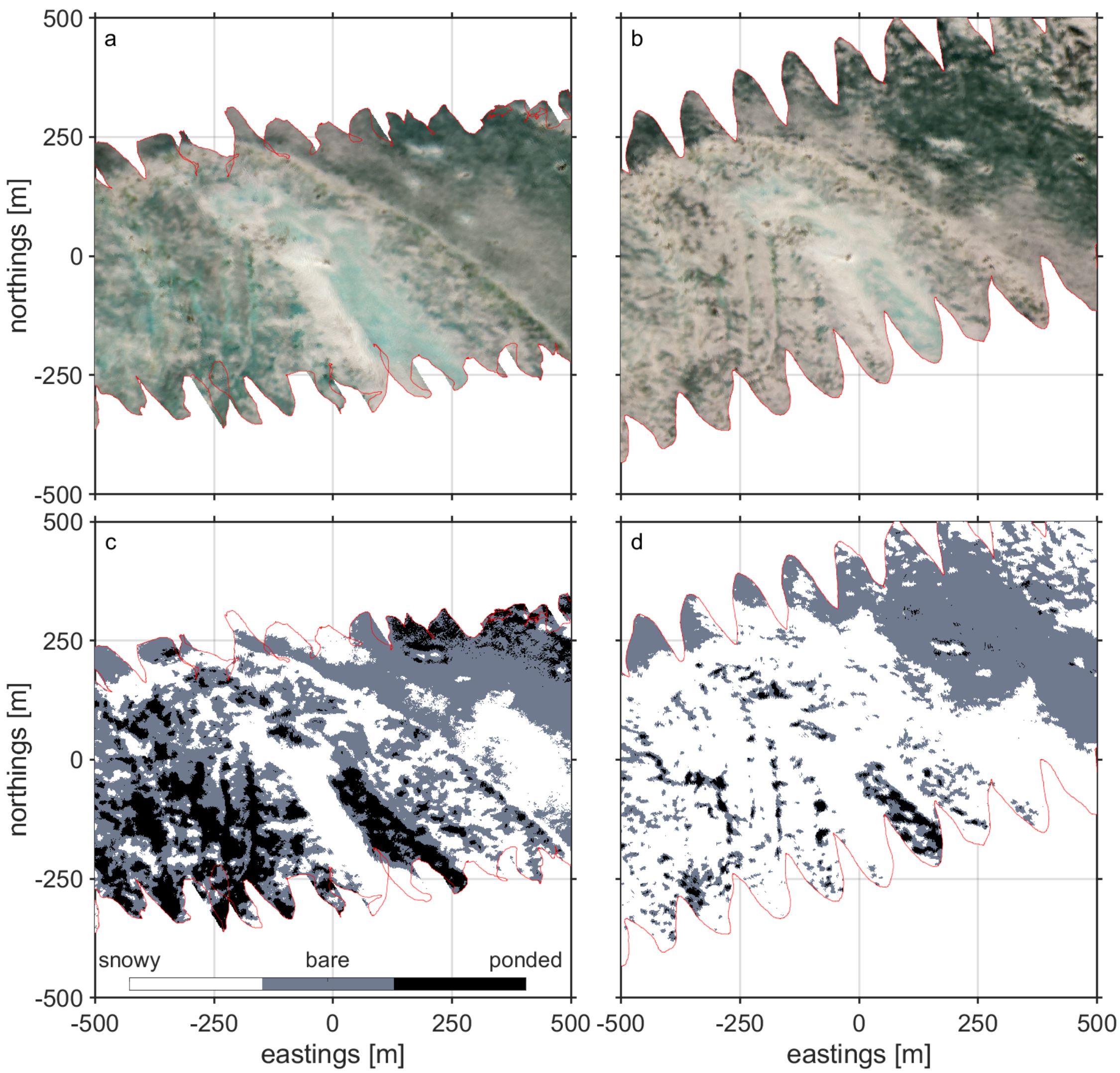

Figure 8: Color mosaics showing the same patch of sea ice from flights on 5/10/2019 (**a**) and 5/14/2019 **(b**). Panels (**c**) and (**d**) provide the corresponding spatial characterizations of surface ice type based on NIR:B and the melt pond detection algorithm of (König & Oppelt, 2020).

This scheme yields a three-level classification, allowing for statistical analysis to be performed on the geometric and radiative characteristics of ponded, bare, and snowy ice features ranging from decimeters to hundreds of meters in length scale. MATLAB's *regionprops* function was used for this processing, yielding the area and perimeter of each detected feature as well as the spectral surface reflectance at each point within each feature. Regions smaller than nine pixels (area < 2.4 m^2) were excluded in order to ensure that feature geometry was not over-constrained by the discretization. Regions larger than 100,000 m^2 were also excluded in order to neglect cases for which the entire field of view was filled with a particular surface type. It is often convenient to reduce the width of the parameter space by representing features in terms of characteristic length scale "*D*" rather than area. Given only the feature area, this may be done via simple square root, assuming the patch is a square: $\boldsymbol{D = \sqrt{area}}$; more realistically, as the diameter of a circle with that area: $\boldsymbol{D = \sqrt{{}^4/_\pi\, area}}$. Given both the feature area and the feature perimeter, one may compute the characteristic length scale $\boldsymbol{D = \frac{4 \cdot area}{perimeter}}$; for a circular feature, *D* becomes the diameter.

3 Results

3.1 Spatially-averaged properties

By combining the observations from consecutive RAD-VNIR flights, it is possible to relate the surface spectral reflectance (and color) to the net solar irradiance. This is shown in Figure 9, with mean visible and near-infrared surface reflectance plotted against net solar irradiance in Figure 9a and the spectral surface reflectance binned by net solar irradiance in Figure 9b. Marker color in Figure 9a was generated from the reflectance in the red, green, and blue bands. Spectrally-flat surfaces (appearing white or gray) are associated with lower net solar irradiance; surfaces colored blue-green are associated with higher net solar irradiance. This is borne out in the binned spectra of Figure 9b, with higher net solar irradiance occurring for lower surface reflectance- but especially lower surface reflectance in the red and near-infared regimes.

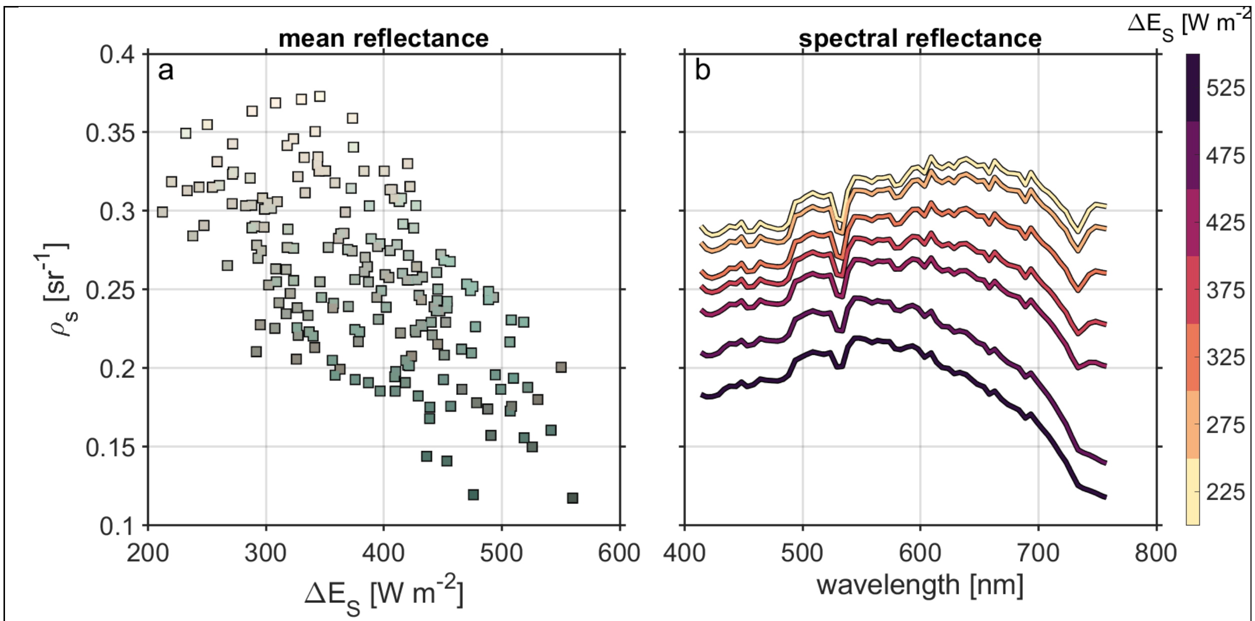

Figure 9: **a** Spatially-averaged surface reflectance ρ_s as a function of net solar irradiance. Marker color corresponds to the surface color determined by the red, green, and blue channels of ρ_s. **b** Spatially-averaged spectral surface reflectance $\rho_s(\lambda)$, with color indicating the bin-averaged net solar irradiance.

3.2 Geometric properties of surface features

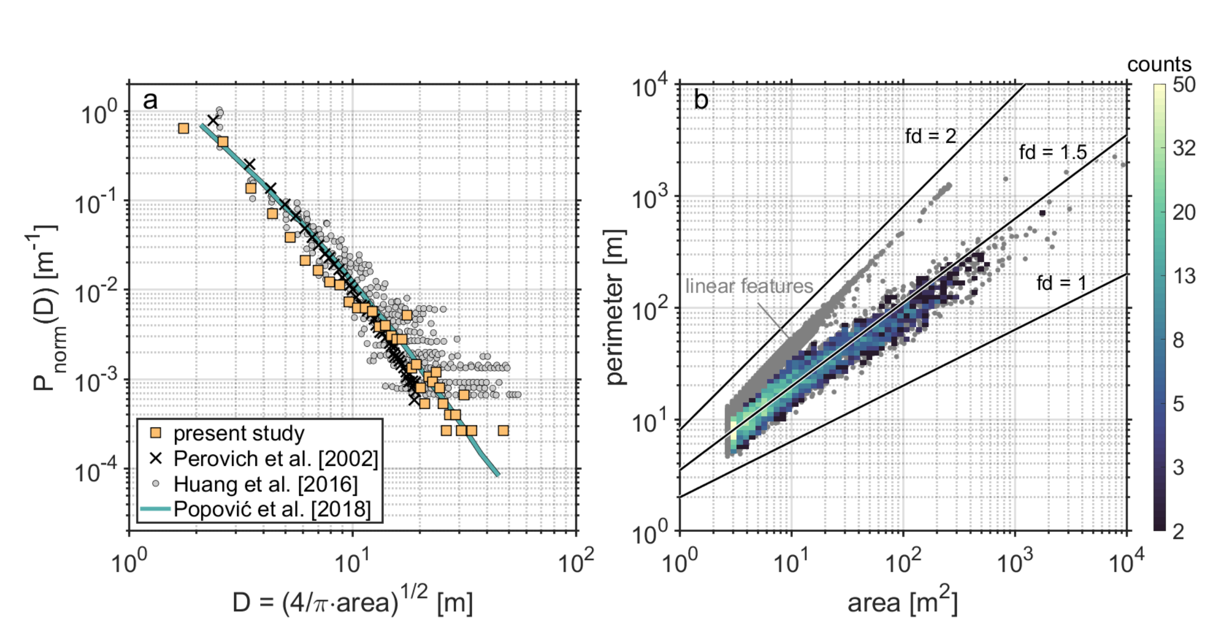

Figure 10: **a** melt pond size probability density functions, represented in terms of the pond effective diameter D. The observational data of (Perovich, Tucker, et al., 2002) and (Huang et al., 2016) are shown alongside the physical model of (Popović et al., 2018) and observational data from the present study. **b** melt pond area-perimeter plot, with individual measurements represented by gray dots and the overlying color indicating the value of the corresponding bivariate histogram. Three lines overlaid on the figure correspond to fractal dimensions of 1, 2, and 1.5, the "pond distribution dimension" defined by (Horvat et al., 2020).

The bulk of section 2.2 was devoted to describing a framework for sea ice feature classification and geometric/radiative analysis. We now show the results of employing that framework. The relationship between area and perimeter offers more than a convenient way of rendering feature length scale- it provides us with information about the fractal dimensionality of the features on the sea ice surface. One such approach for determining fractal dimension (here given as *fd* rather than the literature-standard *D* in order to avoid confusion with our length scale *D*) is the aptly-named area/perimeter relationship (Klinkenberg, 1994): $\boldsymbol{P \propto \left(\sqrt{area}\right)^{fd}}$. In practical terms, *fd* is computed as half the slope of the relationship between $\mathbf{log}\ (\boldsymbol{perimeter})$ and $\mathbf{log}\ (\boldsymbol{area})$; this approach has been applied to melt pond data produced from observations (Hohenegger et al., 2012) and physical geometric modeling (Bowen et al., 2018; Horvat et al., 2020). A value of *fd* = 1 indicates that perimeter scales as the square root of the area (true for non-overlapping simple shapes). In mathematical terms, *fd* = 2 represents a shape-filling curve; in our practical application, *fd* approaching 2 represents linear features that are one ground sample distance wide.

The size distribution and area/perimeter relationship of surface melt ponds are provided in Figure 10; panel a also includes the melt pond size distributions produced from the aerial field observations of (Perovich, Tucker, et al., 2002) and (Huang et al., 2016) and the geometric 'void' model of (Popović et al., 2018), all represented in terms of characteristic length scale $\boldsymbol{D} = \sqrt{{}^{4}/_{\pi}\, \boldsymbol{area}}$.The area/perimeter relationship in panel b is represented with a cloud of gray points indicating individual measurements overlaid with a bivariate histogram that excludes the 'linear features' which bump up against the sensor spatial resolution. The melt pond area/perimeter relationship has been shown to reveal a sigmoid transition in fractal dimension from 1 to 2, with the inflection point tending to occur around a feature area of 100 m^2 (Hohenegger et al., 2012). Our observations do not show this relationship, likely due to the relative paucity of melt pond observations during our field campaign- less than 0.5% of the imaged sea ice surface area contained ponded ice. Indeed, the mean fractal dimension (or, as in (Horvat et al., 2020), 'pond distribution dimension) of ~1.5 appears to indicate that a large fraction of the detected melt ponds had a small area.

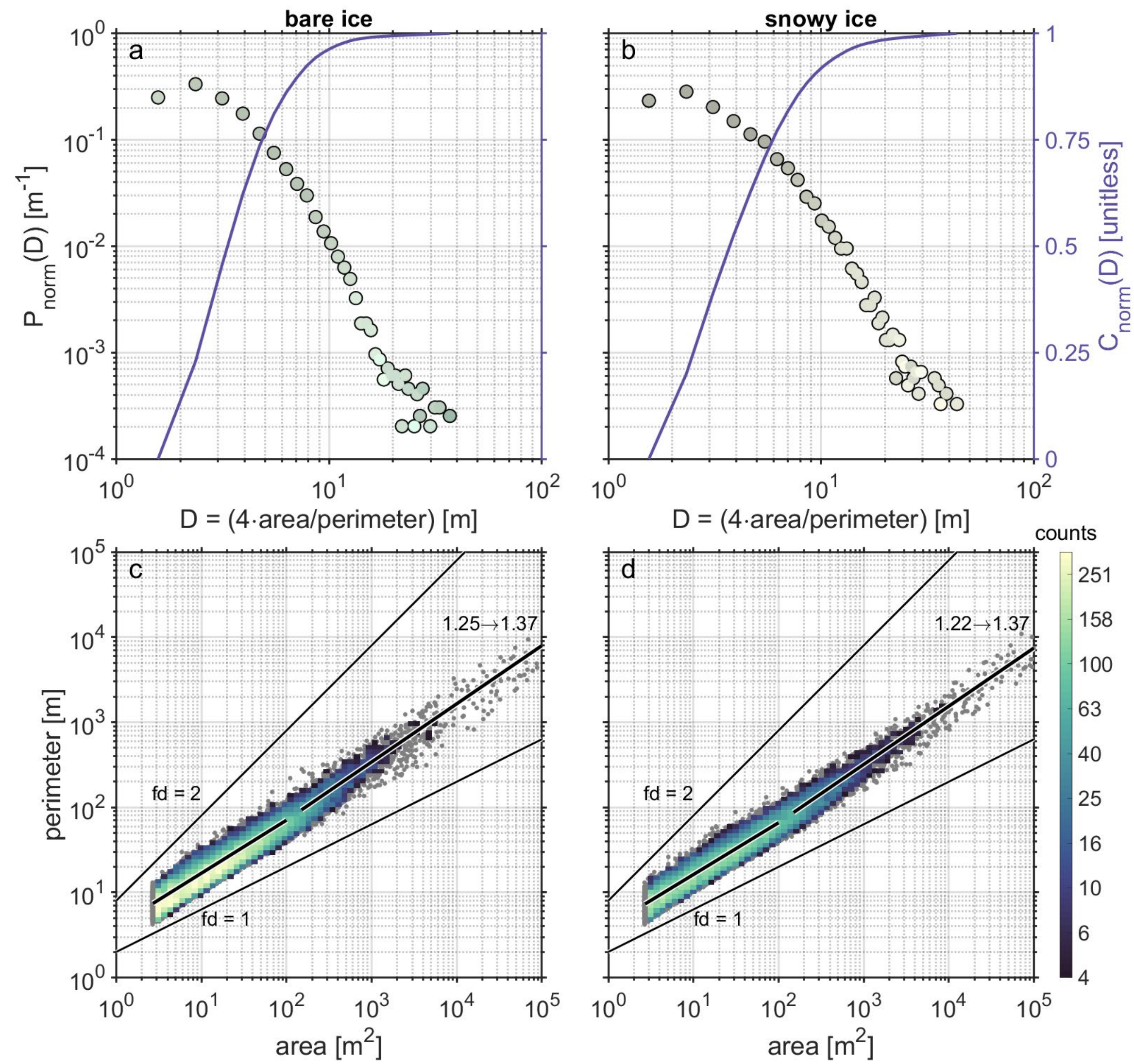

Figure 11: Probability density functions describing snowy ice feature geometry; the layout is generally analogous to that of Figure 10: **a,b** bare and snowy ice feature size probability & cumulative density functions, represented in terms of the pond effective diameter D. Marker color corresponds to the mean feature color for a particular size bin. **c,d** bare and snowy feature area-perimeter plots, with individual measurements represented by gray dots and the overlying color indicating the value of the corresponding bivariate histogram. Two lines overlaid on the figures correspond to fractal dimensions of 1 and 2; the piecewise linear functions correspond to fractal dimensions computed over two regimes: areas ranging from 2.6 m^2 – 100 m^2 and 150 m^2 – 100,000 m^2.

The remaining 99.5% of sea ice surface that was not ponded therefore fell into our two other categories: bare and snowy. The multipanel Figure 11 contains size probability density functions and area/perimeter relationships for bare and snowy ice features. In panels (a-b), we show feature size distributions in terms of characterstic length scale $\boldsymbol{D} = \frac{\boldsymbol{4 \cdot area}}{\boldsymbol{perimeter}}$. There appear to be two regimes in these distributions, with the probability density of large bare or snowy features falling off more steeply with diameter than that of the smaller, darker features. This transition may be analogous to the transition found for melt pond size distributions (Hohenegger et al., 2012; Popović et al., 2018) that follows the sharp increase in fractal dimension as a result of increasing melt pond complexity and connectedness. The geometric bivariate distributions shown in panels (c-d) provide a clearer picture of this transition. For both bare and snowy features, regions smaller than 100 m^2 have fractal dimension *fd* around 1.25 while features larger than 150 m^2 have *fd* around 1.37.

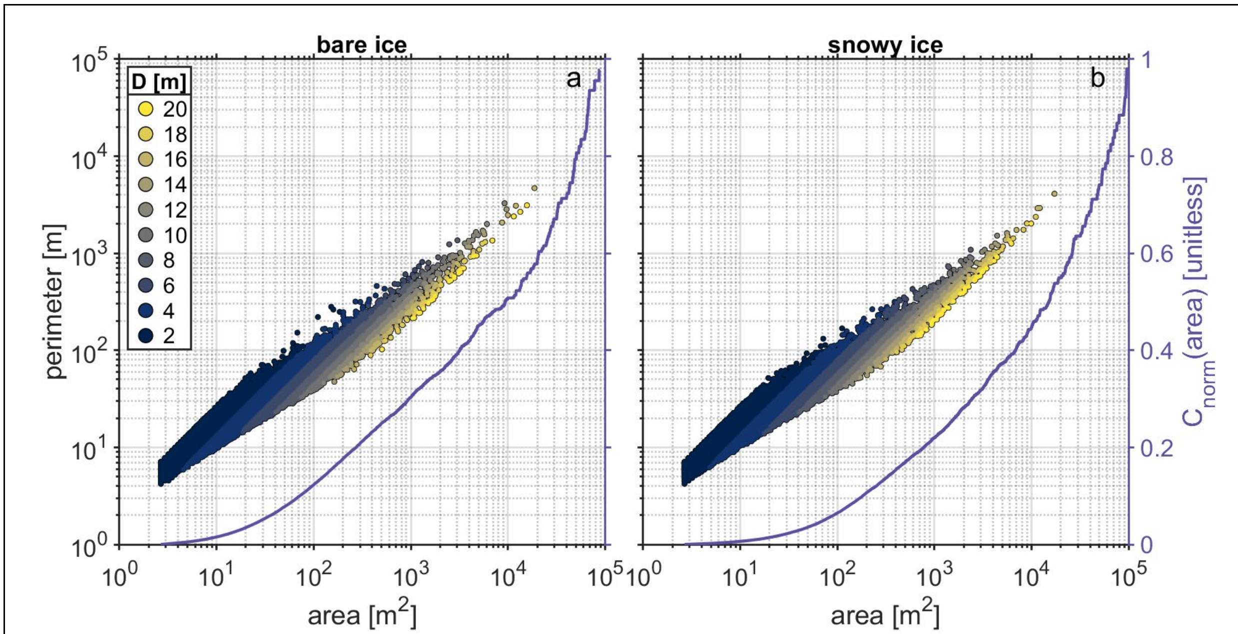

Figure 12: **a,b** Bare and snowy feature area-perimeter plots, with individual marker color corresponding to characteristic feature scale *D*. The violet trace indicates the cumulative density function for feature area.

Although small features dominate the size probability density functions- 99.5% of all bare ice features and 98.5% of all snowy ice features have *D* < 20 m- the majority of the surface is covered by large features. This can be seen in Figure 12; for bare ice, features with characteristic length scale $D < 20$ m occupy only 44% of the total imaged surface. For snowy ice, the same scale range represents only 35% of the total imaged surface.

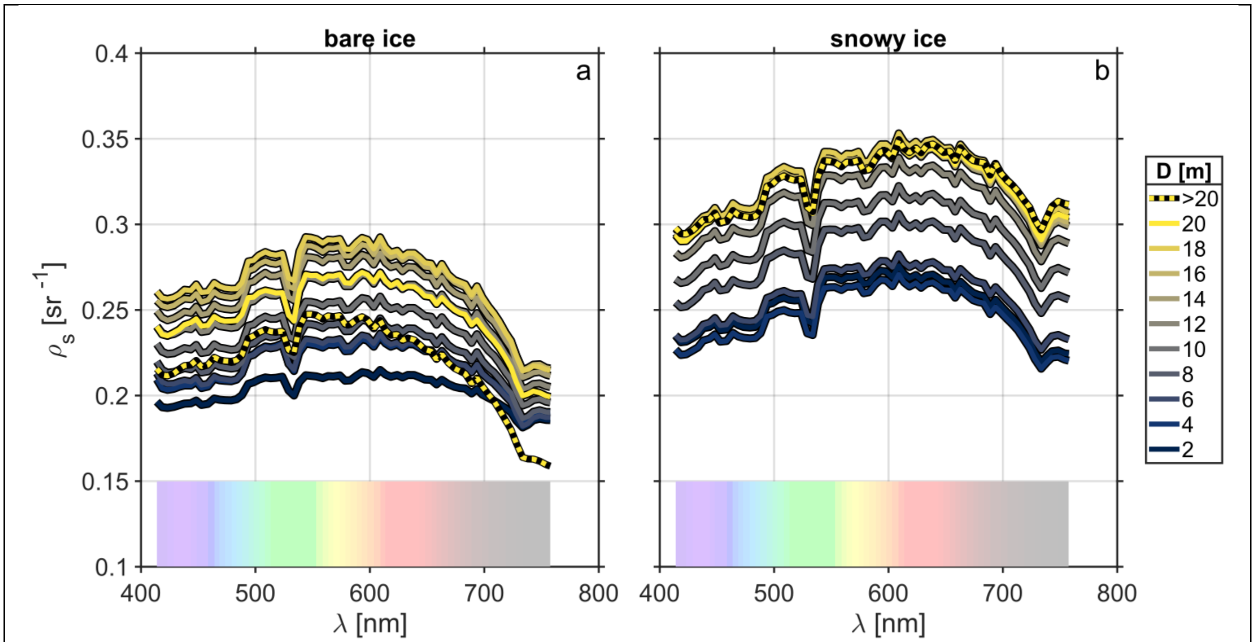

Figure 13: Surface reflectance spectra $\rho_s(\lambda)$ for bare and snowy ice (left and right panels, respectively). The thickness of each trace corresponds to the mean effective feature diameter *D* for which the spectra were bin-averaged. The dotted trace corresponds to the average for $D > 20$ m. The translucent rainbow bar at the base of the plot indicates the approximate color corresponding to each particular wavelength.

From the spatially-averaged reflectance and irradiance shown in Figure 9, we have arrived at the intuitive result that snowy surfaces are of higher total reflectance than bare surfaces-- and that red/near-infrared reflectance is particularly lower for bare ice. Our geometric analysis provides us with the ability to parse this effect by feature size. Figure 13 shows the surface reflectance spectra partitioned by surface type (bare and snowy) and characteristic length scale $\boldsymbol{D} = \sqrt{\frac{\boldsymbol{4 \cdot area}}{\boldsymbol{perimeter}}}$ in bins separated by 2 m (±0.5 m binwidth). The dotted yellow trace indicated by the black asterisk marks the mean spectral reflectance for all features with $D > 20$ m.

3.3 Sub-feature variability

From these spectra, we observe that the spatially-averaged relationships tend to hold at individual scales: for features of a particular size, snowy features will be more reflective than bare features, with bare features especially lower in reflectance at the red/near-infrared wavelengths. However, we also find that the reflectance of snowy ice features tends to vary evenly with size across the visible and near-infrared wavelength range up to $D \approx 14$ m, at which point the spectral reflectance loses sensitivity to feature size and the spectra for $\boldsymbol{D} \gtrsim 14$ m in Figure 13b overlap. Bare ice features behave quite differently (Figure 13a). All reflectance spectra show substantial decline in the near-infrared range, as one might expect from the spatially-averaged spectra shown in Figure 9b and by merit of our very definition of a 'bare' feature (near-infrared to blue spectral reflectance ratio). However, reflectance does not increase monotonically with bare ice feature size; rather, reflectance peaks for features with $D \approx 18$ m- and the spectral reflectance averaged over all features with $D > 20$ m is substantially lower in the near-infared than all other spectra, offering insight into the nature of bare ice radiative signature variation with feature scale.

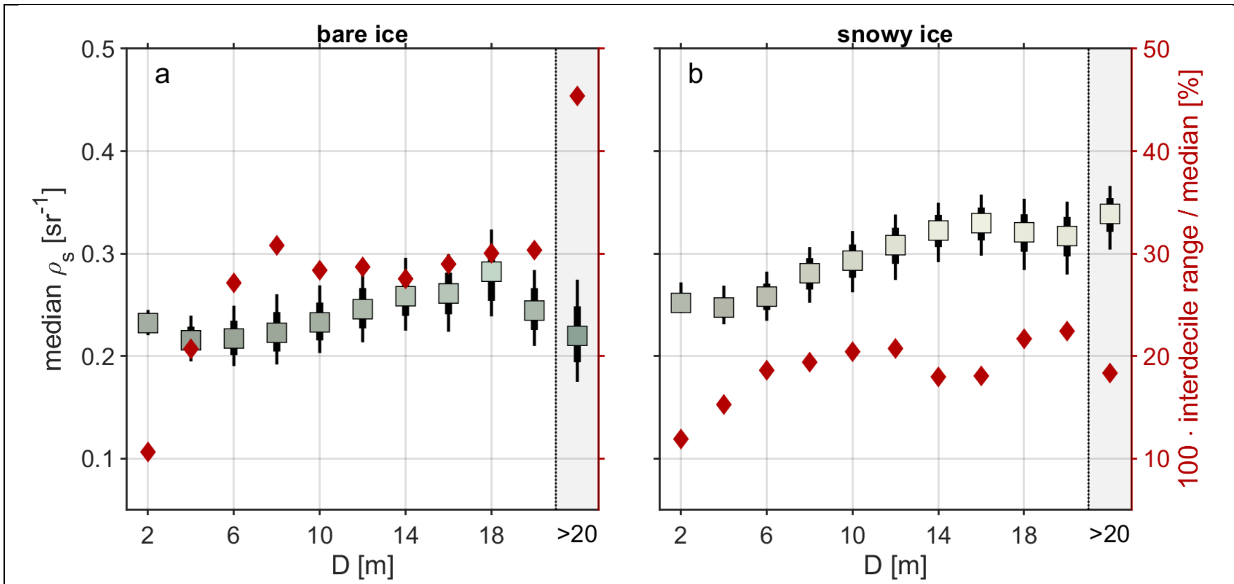

Figure 14: Variation of bare and snowy (**a** & **b**, respectively) ice feature surface reflectance ρ_s with feature size. Marker color indicates the mean feature color; thick and thin vertical lines mark the interquartile and interdecile ranges of ρ_s for each bin. Rust-colored diamonds indicate the ratio between the interdecile range and median value of ρ_s, represented as a percentage. The markers in the gray shaded region represent values computed for all features with $D > 20$ m.

Our 3-class classification scheme simplifies the complex reality of the sea ice surface. In truth, an individually-identified contiguous feature may vary a great deal in its radiative properties over space. In order to describe this variation while keeping the clarifying simplicity of our feature categorization, we computed the inter-percentile (interquartile and interdecile) sub-feature variation as a function of feature scale (Figure 14). We find that variability in spectrally-averaged reflectance is significantly smaller across all features with $\boldsymbol{D < 6}$ **m** than it is across larger features. For larger features ($\boldsymbol{D \geq 6}$ **m**), the variation of spectrally-averaged reflectance is much greater for bare ice than for snowy ice.

4 Discussion

The satellite imagery in Figure 1 shows that the transition of the ice surface from predominantly snow-covered (white) to predominantly bare or ponded (grey or blue-green), a remarkable degree of melt and surface degradation occurred between 5/6/2019 and 5/9/2019, meaning that our aerial observations were made over ice that was in an advanced state of degradation. The relatively warm, moist air mass that arrived in the hours before 5/8/2019 may have been the principal culprit for this change. (Skyllingstad & Polashenski, 2018) found that synoptic weather events transporting warm, moist air over sea ice (and driving sensible/latent heat flux) are the key trigger of incipient surface melt, after which changes to surface albedo result in solar radiation being the principal driver of heat uptake by the sea ice surface. Light transmittance and subsurface light absorption is markedly higher for first-year ice than for multi-year ice (Nicolaus et al., 2013). Furthermore, the sea ice in Kotzebue sound was qualitatively determined to be rich in sediment from the Kobuk and Noatak Rivers. The presence of sediment is understood to greatly enhance the absorption of solar radiation across the visible and near-infrared wavelengths (Perovich, 2017). The absence of multi-year ice, abundance of sediment, and potentially widespread snow ice formations (Mahoney et al, 2021) may all help to explain how the landfast ice progressed from snowy and white to rotten and broken in one week's time.

The radiometric observations performed as part of the present study were parsed along three principal axes: feature type (i.e., ponded ice, snowy ice, and bare ice), feature geometry (i.e., area, perimeter, or some derivative thereof), and wavelength (i.e., in a spectral sense). The simplest form of the results from this work is shown in Figure 9, where the variation of surface reflectance (wavelength-averaged and wavelength-dependent) is displayed as a function of net solar irradiance. The results of Figure 9a are intuitive, and in agreement with the findings of (Yackel et al., 2000): regions with a higher fraction of white/snowy ice have higher total surface reflectance and are associated with lower absorption of solar radiation. The surface reflectance spectra shown in Figure 9b offer a view of sea ice that is analogous to the one presented by (Grenfell & Perovich, 1984), in which measurements of spectral albedo were performed over sea ice with a variety of surface types. For the bare ice and melt pond conditions similar to those observed during our field campaign, there was found to be a steep decline with wavelength for wavelengths between 600-800 nm, with white ice showing a far more gradual decline with wavelength.

Melt ponds draw a great amount of attention in the literature related to sea ice radiative properties- and for good reason. On thick, multi-year ice with persistent snow cover (and therefore generally high albedo across the visible spectrum), melt ponds represent islands of exceptional radiative penetration and under-ice heat absorption. The thin and degraded first-year ice of Kotzebue Sound that served as the subject of our observations in May 2019 held a vanishingly small number of melt ponds: less than 0.5% of the imaged surface area. Although the classification algorithm has been validated via in situ observations by other researchers (König & Oppelt, 2020), we did not perform any ground-truth measurements during our field observational period. It is therefore possible that our approach under-counted melt ponds. This may have impacted our ability to fully characterize melt pond fractal dimension: we did not observe a transition in melt pond fractal dimension from 1 to 2. This transition corresponds to ponds of increasingly serpentine, complex arrangement, and is often observed (Hohenegger et al., 2012) and reproduced via physical modeling (Bowen et al., 2018). Nevertheless, as shown in Figure 10, our observations of the melt pond spatial distribution showed good agreement with previous observations (Huang et al., 2016; Perovich, Tucker, et al., 2002) and the geometric model of (Popović et al., 2018).

The geometric analysis frameworks often applied to melt ponds is in fact well-suited towards the other surface types classified here: snowy & bare ice (Figure 11). For those surface types, we found that small, relatively dark features were most plentiful, with larger and more reflective features somewhat scarce. The behavior in these two feature size clusters appeared to follow two distinct power laws. For snowy features, these are $\boldsymbol{P(D) \propto D^{-1.3}}$ for $\mathbf{2\ m < \boldsymbol{D} < 5\ m}$ and $\boldsymbol{P(D) \propto D^{-3.5}}$ for $\mathbf{10\ m < \boldsymbol{D} < 20\ m}$. The intermediate domain of $\mathbf{5\ m < \boldsymbol{D} < 10\ m}$ corresponds to a range in perimeter of 40 m – 80 m for a feature with area 100 m^2; it is over this span of values that we also observe the transition of fractal dimension from approximately 1.25 to 1.37. This shift indicates that larger, more reflective snowy and bare ice surface features are more complex in shape than smaller, darker features- but only a bit more so. The analogous transition for melt ponds (Bowen et al., 2018; Hohenegger et al., 2012) is quite stark: from fractal dimension just above 1 (very nearly circular ponds) to fractal dimension approaching 2 (very nearly a space-filling curve). This comparison indicates that, while feature complexity of bare and snowy ice surfaces increases with size, it does so only up to a moderate level. This indicates that large features tend to be bulky, with well-defined interior and exterior regions.

The reflectance spectra depicted in Figure 13 offer a more detailed view of these surface feature characteristics. The spectra show an increase in snowy ice reflectance with feature sizes up to $D \approx 14$ m, with larger patches no longer varying with size in spectral reflectance. This is compatible with our previous description of surface features as fairly simple in shape with well-defined interior regions. The observed behavior for bare ice surfaces is quite different, varying non-monotonically with feature size. For bare ice regions, reflectance increases with feature size up to $D \approx 18$ m, only to *decrease* with size (especially in the near-infared range). This reduction appears to become substantial for the features with $D > 20$ m, patches which constitute over 55% of the total observed bare ice by area. As discussed earlier in this section, it may be the case that our classification scheme is under-detecting ponded sea ice. However, the stark difference between snowy and bare reflectance spectra indicate that we are identifying meaningfully different surface types, even if there is some uncertainty regarding the identification of melt ponds.

The sub-region variability in reflectance (Figure 14) provides a complementary description of this distinction. For both bare and snowy surfaces, variability in reflectance increases with scale as features begin to develop fringes, tapering off as darker fringes become a smaller portion of the overall feature area. The scale dependence of this effect appears coincident with the power law and fractal dimension transition scales, shoring up the interpretation that small, loosely-connected regions of uniformly-low reflectance are plentiful. However, these small features still represent a small fraction of the overall sea ice surface area. In order to provide a broader view of the observed sea ice radiative characteristics, it is important to also consider large patches which are few in number but great in total surface area. Snowy ice features increase in mean reflectance (and relative variability) with up to some critical scale at which the patch interior is sufficiently protected from the darker, more absorptive patch fringes. For bare ice features, however, the largest regions which occupy the bulk of the bare ice surface area are darker, of higher variability, and of particularly low reflectivity in the near-infrared. Based on the highly variable reflectance observed for the largest patches, it may be that these regions include cracks, melt water, suspended sediment, and other characteristics which render them vulnerable to increasing absorption of solar radiation.

These findings suggest that surface feature geometry has a meaningful impact on the degree to which sea ice reflects incoming solar radiation. We expect that efforts which seek to model changes to Earth's climate will be advanced by incorporation of these effects, and we eagerly anticipate future studies which investigate the scale-dependence of ice-albedo feedback mechanisms. Indigenous communities who rely on the sea ice as part of their way of life may benefit from such improvements to climate forecasting capabilities. Furthermore, quantification of solar radiation uptake that is dependent upon sea ice color and feature size may assist in the determination of structural safety for use in travel and hunting activities.

5 Conclusions

We performed a series of aerial observations of sea ice radiative properties at an advanced stage of melt and breakup. These observations were performed in Kotzebue Sound, Alaska, and occurred in the context of knowledge co-production with with Elders from Kotzebue (study co-authors J.G., C.H., R.J.S., and R.S., Sr.). This collaboration began with the initial project conception, continuing through execution of observations, and extending into analysis. Our observations allowed us to quantify the mean solar radiative flux into the sea ice as a function of both ice color and spectral surface reflectance. Using high-resolution hyperspectral radiometric imaging, we were able to reconstruct maps of spectral reflectance over the visible to near-infrared range at spatial scales down to 50 cm. This dataset was used to classify the surface into regions of melt ponds, bare ice, and snowy ice and to perform geometric analyses on those regions across the resolved spectrum. Melt ponds were scarce during our operating period, though the ponds we did observe presented with a scale distribution that agreed with that of previous observations and modeling. The spectral reflectance of snowy ice was found to vary with feature size, increasing until moderate scale and then ceasing to vary at all.

These observations of surface reflectance variation offer insight into the role that feature size distribution and geometry play in the overall radiative balance of sea ice. Diminished surface reflectance leads to enhanced uptake of solar radiation, which in turn hastens the degradation (and ultimately, breakup) of the sea ice. We expect that the size and geometry dependence of surface reflectance works to strengthen positive feedbacks associated with radiation uptake. In short: the tendency of large blue-green features to absorb radiation increases with their size, while large snowy features absorb more solar radiation as they are subdivided and split by melt and degradation. We recognize that climate models cannot afford to directly resolve individual features on the sea ice. However, we hope that the effects described in this paper can be parameterized statistically, incorporating scale-aware feedbacks into models without the need for directly resolving individual features.

In closing, these observations provide a quantitative description of the radiative and geometric properties of features on the surface of first-year sea ice undergoing the late stages of melt and breakup. Although the observational period was short, the high spatial and spectral resolutions of the sensing approach deployed here have yielded a rich characterization of the sea ice surface. We anticipate that the results of this work will be used to inform future, larger-scale field observational and modeling efforts aimed at providing a comprehensive description of the sea ice surface properties.

Acknowledgments

This work was supported by a grant from the Gordon and Betty Moore Foundation. We are grateful to the Qikiqtaġruŋmiut people and community of Kotzebue, Alaska. The sharing of their Indigenous Knowledge was an integral part of the design and execution of this work. We thank the Native Village of Kotzebue and the University of Alaska Fairbanks (Chukchi campus) who provided meeting facilities and the US Fish and Wildlife Selawik Refuge, who provided crucial logistical support. We thank Scott Brown, Tej Dhakal, and Ryan Harris for their engineering expertise in the development and field operation of the scientific payloads. We thank Cory Rosene, Scott Bowers, and Sean Culbertson for their work in piloting and maintaining the aircraft. Historical meteorological data from the Kotzebue airport were obtained from the National Centers for Environmental Information at https://www.ncdc.noaa.gov/cdo-web/datasets/LCD/stations/WBAN:26616/detail. The terrestrial and UAV-obtained datasets (as well as all computer codes used to process them to produce the figures shown in this document) are available through the Columbia Academic Commons (DOI: 10.7916/rrbv-k026). The authors declare that they have no competing financial interests.

Appendix

The TSPI solution produced through post-processing of data obtained from the Base payload's INU provided the aircraft position and attitude at 50 Hz. This was interpolated onto the time vector of the radiometric instrumentation of the VNIR payload. Three attitude angles- pitch, roll, and yaw- are shown in Figure A1a; note that the yaw angle represents variation about the mean heading. An RGB representation of 60 seconds' worth of calibrated (but not georectified) surface reflectance data is shown in Figure A1b. Vectors originating from the camera focal point and terminating at each point in this array were initialized; the position corresponding to each spatial measurement of surface reflectance was determined by rotating each vector by the instantaneous UAV attitude in three dimensions and finding its intersection with the ellipsoid defining the mean ocean surface. The output of this process is shown in Figure A1c. Another illustration of this VNIR pushbroom orthrectification is provided by (Zappa et al., 2020).

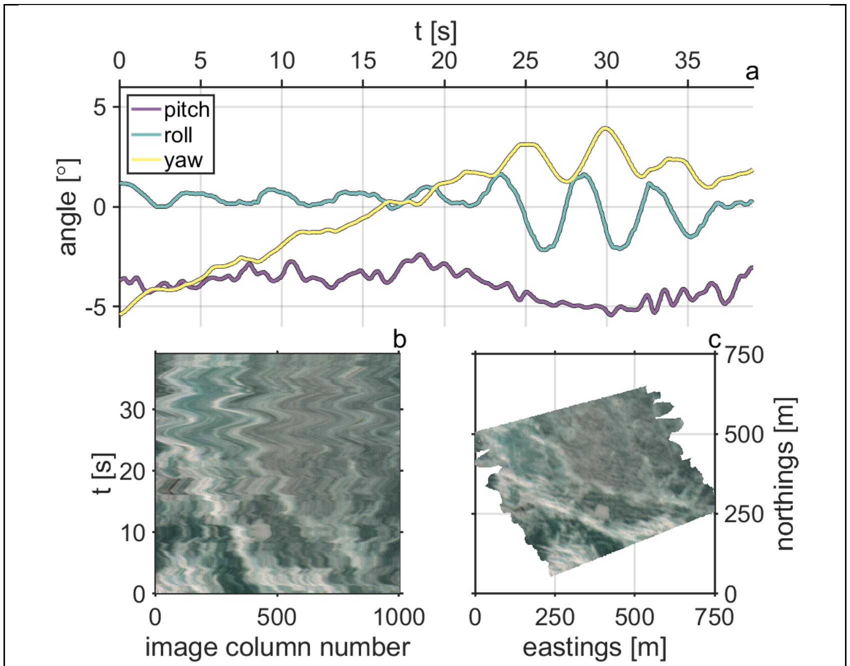

Figure A1: Demonstration of the orthorectification process undertaken for the VNIR payload's pushbroom imager. (**a**) Sample time series of the aircraft's pitch, roll, and yaw angles over a 40-second segment. (**b**) Color image produced from the red, green, and blue channels of ρ_s. (**c**) Orthorectified color mosaic.

References

Barber, D. G., & Yackel, J. (2010). The physical, radiative and microwave scattering characteristics of melt ponds on Arctic landfast sea ice. *International Journal of Remote Sensing*, *20*(10), 2069–2090. https://doi.org/10.1080/014311699212353

Bourassa, M. A., Gille, S. T., Bitz, C., Carlson, D., Cerovecki, I., Clayson, C. A., et al. (2013). High-Latitude Ocean and Sea Ice Surface Fluxes: Challenges for Climate Research. *Bulletin of the American Meteorological Society*, *94*(3), 403–423. https://doi.org/10.1175/BAMS-D-11-00244.1

Bowen, B., Strong, C., & Golden, K. M. (2018). Modeling the fractal geometry of Arctic melt ponds using the level sets of random surfaces. *Journal of Fractal Geometry*, *5*(2), 121–142. https://doi.org/10.4171/JFG/58

Bremer, S., Wardekker, A., Dessai, S., Sobolowski, S., Slaattelid, R., & van der Sluijs, J. (2019). Toward a multi-faceted conception of co-production of climate services. *Climate Services*, *13*, 42–50. https://doi.org/10.1016/J.CLISER.2019.01.003

Brennan, M. K., Hakim, G. J., & Blanchard-Wrigglesworth, E. (2020). Arctic Sea-Ice Variability During the Instrumental Era. *Geophysical Research Letters*, *47*(7), e2019GL086843. https://doi.org/10.1029/2019GL086843

Budyko, M. I. (1969). The effect of solar radiation variations on the climate of the Earth. *Tellus*, *21*(5).

Carmack, E., Polyakov, I., Padman, L., Fer, I., Hunke, E., Hutchings, J., et al. (2015). Toward Quantifying the Increasing Role of Oceanic Heat in Sea Ice Loss in the New Arctic. *Bulletin of the American Meteorological Society*, *96*(12), 2079–2105. https://doi.org/10.1175/BAMS-D-13-00177.1

Dai, A., Luo, D., Song, M., & Liu, J. (2019). Arctic amplification is caused by sea-ice loss under increasing CO 2. *Nature Communications 2019 10:1*, *10*(1), 1–13. https://doi.org/10.1038/s41467-018-07954-9

David-Chavez, D. M., & Gavin, M. C. (2018). A global assessment of Indigenous community engagement in climate research. *Environmental Research Letters*, *13*(12), 123005. https://doi.org/10.1088/1748-9326/AAF300

Ehn, J. K., Mundy, C. J., Barber, D. G., Hop, H., Rossnagel, A., & Stewart, J. (2011). Impact of horizontal spreading on light propagation in melt pond covered seasonal sea ice in the Canadian Arctic. *Journal of Geophysical Research: Oceans*, *116*(C9), 0–02. https://doi.org/10.1029/2010JC006908

Eicken, H. (2010). Indigenous Knowledge and Sea Ice Science: What Can We Learn from Indigenous Ice Users? *SIKU: Knowing Our Ice: Documenting Inuit Sea Ice Knowledge and Use*, 357–376. https://doi.org/10.1007/978-90-481-8587-0_15

Eicken, H., Danielsen, F., Sam, J.-M., Fidel, M., Johnson, N., Poulsen, M. K., et al. (2021). Connecting Top-Down and Bottom-Up Approaches in Environmental Observing. *BioScience*, *71*(5), 467–483. https://doi.org/10.1093/BIOSCI/BIAB018

Frey, K. E., Perovich, D. K., & Light, B. (2011). The spatial distribution of solar radiation under a melting Arctic sea ice cover. *Geophysical Research Letters*, *38*(22). https://doi.org/10.1029/2011GL049421

Gearheard, S. F., Leavitt, J. M., Mahoney, A. R., Opie, M., Oshima, T., & Sanguya, J. (Eds.). (2013). *The Meaning of Ice: People and Sea Ice in Three Arctic Communities*. International Polar Institute Press.

Grenfell, T. C., & Perovich, D. K. (1984). Spectral albedos of sea ice and incident solar irradiance in the southern Beaufort Sea. *Journal of Geophysical Research: Oceans*, *89*(C3), 3573–3580. https://doi.org/10.1029/JC089IC03P03573

Grenfell, T. C., & Perovich, D. K. (2004). Seasonal and spatial evolution of albedo in a snow-ice-land-ocean environment. *Journal of Geophysical Research: Oceans*, *109*(C1), 1001. https://doi.org/10.1029/2003JC001866

Hauser, D. D. W., Whiting, A. V., Mahoney, A. R., Goodwin, J., Harris, C., Schaeffer, R. J., et al. (2021). Co-production of knowledge reveals loss of Indigenous hunting opportunities in the face of accelerating Arctic climate change. *Environmental Research Letters*, *16*(9), 095003. https://doi.org/10.1088/1748-9326/AC1A36

Hohenegger, C., Alali, B., Steffen, K. R., Perovich, D. K., & Golden, K. M. (2012). Transition in the fractal geometry of Arctic melt ponds. *The Cryosphere*, *6*(5), 1157–1162. https://doi.org/10.5194/tc-6-1157-2012

Horvat, C., Flocco, D., Rees Jones, D. W., Roach, L., & Golden, K. M. (2020). The Effect of Melt Pond Geometry on the Distribution of Solar Energy Under First-Year Sea Ice. *Geophysical Research Letters*, *47*(4), e2019GL085956. https://doi.org/10.1029/2019GL085956

Huang, W., Lu, P., Lei, R., Xie, H., & Li, Z. (2016). Melt pond distribution and geometry in high Arctic sea ice derived from aerial investigations. *Annals of Glaciology*, *57*(73), 105–118. https://doi.org/10.1017/AOG.2016.30

Klenk, N., Fiume, A., Meehan, K., & Gibbes, C. (2017). Local knowledge in climate adaptation research: moving knowledge frameworks from extraction to co-production. *Wiley Interdisciplinary Reviews: Climate Change*, *8*(5), e475. https://doi.org/10.1002/WCC.475

Klinkenberg, B. (1994). A review of methods used to determine the fractal dimension of linear features. *Mathematical Geology*, *26*(1), 23–46. https://doi.org/10.1007/BF02065874

König, M., & Oppelt, N. (2020). A linear model to derive melt pond depth on Arctic sea ice from hyperspectral data. *Cryosphere*, *14*(8), 2567–2579. https://doi.org/10.5194/TC-14-2567-2020

Kwok, R., & Rothrock, D. A. (2009). Decline in Arctic sea ice thickness from submarine and ICESat records: 1958–2008. *Geophysical Research Letters*, *36*(15). https://doi.org/10.1029/2009GL039035

Light, B., Grenfell, T. C., & Perovich, D. K. (2008). Transmission and absorption of solar radiation by Arctic sea ice during the melt season. *Journal of Geophysical Research: Oceans*, *113*(C3), 3023. https://doi.org/10.1029/2006JC003977

Light, B., Perovich, D. K., Webster, M. A., Polashenski, C., & Dadic, R. (2015). Optical properties of melting first-year Arctic sea ice. *Journal of Geophysical Research: Oceans*, *120*(11), 7657–7675. https://doi.org/10.1002/2015JC011163

Lindsay, J. M., Hauser, D. D. W., Mahoney, A. R., Laidre, K. L., Goodwin, J., Harris, C., et al. (2023). Characteristics of ringed seal Pusa hispida ('natchiq') denning habitat in Kotzebue Sound, Alaska, during a year of limited sea ice and snow. *Marine Ecology Progress Series*, *705*, 1–20. https://doi.org/10.3354/meps14252

Lu, P., Leppäranta, M., Cheng, B., & Li, Z. (2016). Influence of melt-pond depth and ice thickness on Arctic sea-ice albedo and light transmittance. *Cold Regions Science and Technology*, *124*, 1–10. https://doi.org/10.1016/J.COLDREGIONS.2015.12.010

Mahoney, A. R., Turner, K. E., Hauser, D. D. W., Laxague, N. J. M., Lindsay, J. M., Whiting, A. V., et al. (2021). Thin ice, deep snow and surface flooding in Kotzebue Sound: landfast ice mass balance during two anomalously warm winters and implications for marine mammals and subsistence hunting. *Journal of Glaciology*, *67*(266), 1013–1027. https://doi.org/10.1017/JOG.2021.49

Markus, T., Stroeve, J. C., & Miller, J. (2009). Recent changes in Arctic sea ice melt onset, freezeup, and melt season length. *Journal of Geophysical Research: Oceans*, *114*(C12), 12024. https://doi.org/10.1029/2009JC005436

Nicolaus, M., Arndt, S., Katlein, C., Maslanik, J., & Hendricks, S. (2013). Changes in Arctic sea ice result in increasing light transmittance and absorption. *Geophysical Research Letters*, *40*(11), 2699–2700. https://doi.org/10.1002/GRL.50523

Overland, J. E. (2020). Less climatic resilience in the Arctic. *Weather and Climate Extremes*, *30*, 100275. https://doi.org/10.1016/J.WACE.2020.100275

Perovich, D. K. (2017). Sea ice and sunlight. *Sea Ice: Third Edition*, 110–137. https://doi.org/10.1002/9781118778371.CH4

Perovich, D. K., & Polashenski, C. (2012). Albedo evolution of seasonal Arctic sea ice. *Geophysical Research Letters*, *39*(8), 8501. https://doi.org/10.1029/2012GL051432

Perovich, D. K., Roesler, C. S., & Pegau, W. S. (1998). Variability in Arctic sea ice optical properties. *Journal of Geophysical Research: Oceans*, *103*(C1), 1193–1208. https://doi.org/10.1029/97JC01614

Perovich, D. K., Tucker, W. B., & Ligett, K. A. (2002). Aerial observations of the evolution of ice surface conditions during summer. *Journal of Geophysical Research: Oceans*, *107*(C10), SHE 24-1. https://doi.org/10.1029/2000JC000449

Perovich, D. K., Grenfell, T. C., Light, B., & Hobbs, P. V. (2002). Seasonal evolution of the albedo of multiyear Arctic sea ice. *Journal of Geophysical Research: Oceans*, *107*(C10), SHE 20-1. https://doi.org/10.1029/2000JC000438

Perovich, D. K., Light, B., & Dickinson, S. (2020). Changing ice and changing light: trends in solar heat input to the upper Arctic ocean from 1988 to 2014. *Annals of Glaciology*, *61*(83), 401–407. https://doi.org/10.1017/AOG.2020.62

Planck, C. J., Perovich, D. K., & Light, B. (2020). A Synthesis of Observations and Models to Assess the Time Series of Sea Ice Mass Balance in the Beaufort Sea. *Journal of Geophysical Research: Oceans*, *125*(11), e2019JC015833. https://doi.org/10.1029/2019JC015833

Popović, P., Cael, B. B., Silber, M., & Abbot, D. S. (2018). Simple Rules Govern the Patterns of Arctic Sea Ice Melt Ponds. *Physical Review Letters*, *120*(14), 148701. https://doi.org/10.1103/PhysRevLett.120.148701

Rantanen, M., Karpechko, A. Y., Lipponen, A., Nordling, K., Hyvärinen, O., Ruosteenoja, K., et al. (2022). The Arctic has warmed nearly four times faster than the globe since 1979. *Communications Earth & Environment*, *3*(1), 1–10. https://doi.org/10.1038/s43247-022-00498-3

Screen, J. A., & Simmonds, I. (2010). The central role of diminishing sea ice in recent Arctic temperature amplification. *Nature*, *464*(7293), 1334–1337. https://doi.org/10.1038/nature09051

Skyllingstad, E. D., & Polashenski, C. (2018). Estimated Heat Budget During Summer Melt of Arctic First-Year Sea Ice. *Geophysical Research Letters*, *45*(21), 11,789-11,797. https://doi.org/10.1029/2018GL080349

Stroeve, J. C., Markus, T., Boisvert, L., Miller, J., & Barrett, A. (2014). Changes in Arctic melt season and implications for sea ice loss. *Geophysical Research Letters*, *41*(4), 1216–1225. https://doi.org/10.1002/2013GL058951

Witte, C. R., Zappa, C. J., Mahoney, A. R., Goodwin, J., Harris, C., Schaeffer, R. J., et al. (2021). The Winter Heat Budget of Sea Ice in Kotzebue Sound: Residual Ocean Heat and the Seasonal Roles of River Outflow. *Journal of Geophysical Research: Oceans*, *126*(9), e2020JC016784. https://doi.org/10.1029/2020JC016784

Wright, N. C., & Polashenski, C. M. (2018). Open-source algorithm for detecting sea ice surface features in high-resolution optical imagery. *The Cryosphere*, *12*(4), 1307–1329. https://doi.org/10.5194/tc-12-1307-2018

Yackel, J. J., Barber, D. G., & Hanesiak, J. M. (2000). Melt ponds on sea ice in the Canadian Archipelago: 1. Variability in morphological and radiative properties. *Journal of Geophysical Research: Oceans*, *105*(C9), 22049–22060. https://doi.org/10.1029/2000JC900075

Yua, E., Raymond-Yakoubian, J., Daniel, R., & Behe, C. (2022). A framework for co-production of knowledge in the context of Arctic research. *Ecology and Society*, *27*(1). https://doi.org/10.5751/ES-12960-270134

Zappa, C. J., Brown, S. M., Laxague, N. J. M., Dhakal, T., Harris, R. A., Farber, A. M., & Subramaniam, A. (2020). Using Ship-Deployed High-Endurance Unmanned Aerial Vehicles for the Study of Ocean Surface and Atmospheric Boundary Layer Processes. *Frontiers in Marine Science*, *6*, 777. https://doi.org/10.3389/fmars.2019.00777